Journal of Alloys and Compounds 1029 (2025) 180732

Contents lists available at ScienceDirect

Journal of Alloys and Compounds

journal homepage: www.elsevier.com/locate/jalcom

Characterization of Cu-Nb-Cu heterostructure fabricated by high-pressure torsion

Tahereh Zargar [a,*], Fazlollah Sadeghi [b], Tayebeh Mousavi [a], Solène Planat [c], Serkan Öğüt [d], Yi Huang [e], Terence G. Langdon [f]

[a] Department of Engineering, King's College London, London WC2R 2LS, UK
[b] Brunel Centre for Advanced Solidification (BCAST), Brunel University, Middlesex, London UB8 3PH, UK
[c] Polytech Paris-Saclay, Paris-Saclay University, Orsay 91190, France
[d] Department of Mechanical Engineering, Faculty of Engineering, Marmara University, Maltepe, İstanbul 34854, Turkey
[e] Department of Design and Engineering, Faculty of Science and Technology, Bournemouth University, Poole, Dorset BH12 5BB, UK
[f] Departments of Aerospace & Mechanical Engineering and Materials Science, University of Southern California, Los Angeles, CA 90089-1453, USA

ARTICLE INFO

Keywords:
Composites
Cu-Nb-Cu heterostructures
High-pressure torsion
Mechanical properties
Microstructural characterization
Severe plastic deformation

ABSTRACT

High-pressure torsion (HPT) processing disrupts the thermodynamic equilibrium in immiscible systems and often produces nonequilibrium microstructures with unique properties. This study investigates the microstructural evolution and mechanical behaviour of a Cu-Nb immiscible alloy subjected to HPT under 6 GPa compressive stress. The HPT processing was performed on stacked Cu-Nb-Cu layers by up to 200 turns and this produced mechanically alloyed, homogenized disks free of porosity or cavities. Microstructural characterization using X-ray diffraction and scanning electron microscopy, coupled with energy-dispersive X-ray spectroscopy, revealed a stepwise evolution, including the reduction of segregation layers, the formation of nonequilibrium Cu-17 at%Nb solid solution in the disc processed at 200 HPT turns and an increased Nb insertion into the Cu lattice. Additionally, grain refinement and residual strain increments were observed with increasing torsional turns. Thereafter, the mechanical properties were evaluated using hardness mapping and tensile testing. The material exhibited strain hardening behaviour and achieved an ultimate tensile strength (UTS) exceeding 1.25 GPa. Following post-deformation annealing, the UTS decreased to ~700 MPa due to recrystallization and recovery. These results provide a preliminary understanding of microstructural transformations and their impact on the mechanical properties of immiscible systems subjected to extreme deformation.

1. Introduction

Processing through the application of severe plastic deformation (SPD) has attracted much attention over the last three decades [1–4], primarily because of the early demonstration that the use of SPD provides the capability of producing materials having submicrometer or even nanometer grain sizes [5]. Processing by SPD refers to the imposition of exceptionally high strains but without incurring any significant changes in the overall dimensions of the workpieces. Several different SPD processing routes are now available but the major techniques are equal-channel angular pressing (ECAP) [6,7] where a rod or bar is pressed repetitively through a die contained within a channel bent through a sharp angle, accumulative roll-bonding (ARB) [8–11] where a plate is rolled repetitively to one half thickness and then cut in half, degreased and wire brushed, stacked, and then rolled again and high-pressure torsion (HPT) [12–15] where a small sample, usually in the form of a disk, is subjected to a high pressure and concurrent torsional straining. In practice, HPT is especially attractive because it is a continuous process not requiring any additional labour within the straining operation. Furthermore, by using HPT to consolidate disk specimens in a single operation it is possible to produce bulk-state reactions and hybrid metals having unusual and exceptional properties [16,17]. This approach to HPT was first developed using a half-disk setup [18], then a quarter-disk setup [19] and more recently through stacking disks in a sandwich-type array [20–22].

Among the various hybrid systems examined to date, copper has been used extensively as a matrix material due to its ductility, formability and high thermal conductivity at room temperature [23–25]. In

* Corresponding author.
E-mail address: tahereh.zargar@kcl.ac.uk (T. Zargar).

https://doi.org/10.1016/j.jallcom.2025.180732
Received 21 January 2025; Received in revised form 21 April 2025; Accepted 1 May 2025
Available online 2 May 2025

addition, due to the very low solubility of binary metals such as Cu-Ta [24,26], Cu-Al [23] and Cu-Ag [27], it is possible to form a non-equilibrium homogeneous binary alloy with an ultrafine grain structure across the whole specimen. Among the immiscible alloying systems that are mechanically produced via ball milling, the Cu-Nb has also attracted much attention [28–34] due to the exceptional mechanical, electrical, and thermal properties, making it highly relevant for applications in nanostructured materials, high-strength conductors and radiation-resistant components. Furthermore, the almost negligible solubility of Nb into Cu at equilibrium conditions, the high formability of Cu and the large difference in atomic sizes of Cu and Nb make the Cu-Nb system an ideal candidate for investigating solid solution alloying under SPD. Studying this system provides insights into the manner in which the application of extreme deformation can enhance solubility beyond the equilibrium limits, thereby leading to potential advancements in material design. In addition, in many immiscible alloying systems a complete solubility cannot be achieved but the nano-scale distribution of immiscible phases leads to a sharp enhancement in the mechanical properties. Thus, it is possible to mechanically alloy the two metals and apply a subsequent annealing heat treatment to produce precipitates that contribute to precipitation hardening.

In the ball milling process, the powders of two metals are mechanically mixed together for a relatively long time to form an alloyed powder such as Cu-Nb [28–30,34–36]. This is typically followed by high-temperature consolidation to obtain a solid form. However, the existence of oxygen during the ball milling process induces oxidation into the alloy which leads to the formation of undesirable phases and results in a deterioration in the mechanical properties with the final product usually containing internal voids. By studying the stable Nb-oxide particles formed during powder alloying, it was demonstrated that there is a challenging effect of such particles on the kinetics and microstructure after heat treatment [37]. By contrast, the HPT process is capable of forming a mixed alloy composed of metals with almost zero solubility at room temperature (RT) [26]. The HPT is accompanied by a large torsion where an applied strain is induced in the material under a high compressive pressure. The advantage of HPT is the potential for avoiding oxidation because the experiments may be conducted at room temperature in air. Additionally, the high compressive pressure, in the range of several GPa, provides the driving force for mechanical alloying as well as preventing porosity and crack formation.

Despite the extensive research undertaken in the fabrication of Cu-Nb alloys for high mechanical properties, the issues associated with the mechanical ball milling process produce relatively poor mechanical properties. For this reason, in the present research an attempt was made to fabricate a Cu-Nb nanostructured alloy using the HPT process which leads to the production of a bulk alloy sheet without introducing oxides, pores and/or cracks. An analysis was performed on the effect of the numbers of turns in producing homogeneity in the alloy mixture, followed by microstructural characterization and an evaluation of the mechanical properties. Analyzing the samples after an annealing heat treatment was conducted finally and the microstructural features were characterized.

2. Experimental procedures

HPT experiments were carried out at room temperature on the samples through numbers of turns of 0.25, 5, 10, 20, 50, 100 and 200. The 0.25 test was performed as representative of almost no turns where the specimen is subjected only to compression. Before the HPT processing the Cu and Nb disks had a diameter of 10 mm and a thickness of 1 mm. The specimen configuration used for HPT processing consisted of a single niobium disk sandwiched between two Cu disks which were compressed at an applied pressure of 6.0 GPa with the bottom anvil rotating at 1 rpm as shown in Fig. 1. Each HPT anvil had a diameter of 10 mm and a cavity depth of about 0.25 mm, which means that the sample is processed under quasi-constrained conditions where there is a small outflow of material around the periphery during the HPT processing [38]. In order to avoid any problems associated with slippage during the processing operation, all of the HPT processing was conducted using new anvils so that the surfaces within the cavity were in perfect condition and had enough frictional force to hold the processed disk sample during rotation. In addition, some preliminary tests were conducted using the standard practice [39] where the Cu and Nb disks were scribed with marker lines on the top and bottom surfaces and these tests revealed no evidence for any slippage under the present experimental conditions. The temperature rise during HPT processing is proportional to the sample strength, applied pressure and the rotation rate [40]. With a rotation speed of 1 rpm and applied pressure of 6.0 GPa, typically temperature rises ranging from 5 to 50°C are recorded for various alloys and pure metals [41,42]. It is estimated, therefore, that the temperature rise during HPT processing of the Cu-Nb alloy should be not more than 50°C. After HPT processing, the HPT-processed Cu-Nb specimens had a diameter of 10 mm and a thickness of ~0.8 mm. Post-deformation annealing heat treatments were performed on the 200 turns sample with annealing temperatures at 973 and 1173 K for 60 minutes.

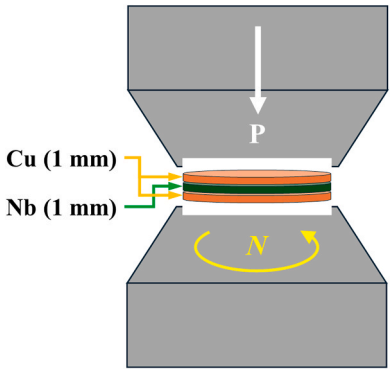

Fig. 1. Schematic illustration of the quasi-constrained HPT condition.

X-ray diffraction (XRD) was conducted on a Rigaku MiniFlex 600 machine which utilizes a Cu Kα monochromatic beam (wavelength $\lambda = 0.154$ nm) at 40 kV and a tube current of 15 mA. The XRD measurements were carried out between 2θ of 10° to 100° with a 0.05° step size at a scanning speed of $5°\text{min}^{-1}$ and the XRD patterns were then analyzed to measure crystallite size and lattice strain of each Cu and Nb using the conventional Williamson-Hall equation [43]. Then, for the microstructural characterization, the cross-sections of the disks were mounted, ground and polished followed by optical microscopy imaging throughout the whole section. A Zeiss EVO LS15 scanning electron microscope (SEM) and Oxford Instruments Energy-Dispersive X-Ray Spectroscopy (EDS) were used for back scattered electron (BSE) imaging of the samples followed by elemental analysis at 20 keV and 1000 pA probe current for taking BSE images and 200 pA probe current for EDS mapping and line scanning at 8.5 mm working distance. High-resolution microstructural analysis was carried out using a transmission electron microscope (TEM, JEOL3000F) on cross-sectional samples made by the lift-out technique in focused ion beam (FIB) milling.

The mechanical properties were investigated using a Zwick Z030 Proline testing machine with a strain rate of $1.0 \times 10^{-3}\ \text{s}^{-1}$ at room temperature. Thus, two off-center miniature tensile specimens were machined from each HPT sample using electrical discharge wire cutting. Dog-bone tensile specimens were cut from the HPT samples at the $N = 200$ turns condition and with a post-HPT annealing condition. The tensile specimens had gauge widths and gauge lengths of ~1.0 and ~1.1 mm, respectively. The tensile tests were conducted at least in duplicate for each condition (HPT-processed and post-HPT annealing) to ensure the reproducibility of the results. Additionally, the hardness mapping was performed on the cross-sections of the HPT-processed

0.25, 10, 50, 100 and 200 turns samples. Vickers hardness measurements were recorded using an FM300 microhardness tester under a load of ~200 gf and a dwell time of 15 s. Separate measurements were carried out at points along the disk diameters from the bottom to the top of the cross-section. This hardness mapping represents the overall hardness distribution over the whole cross-sectional area. The minimum distance between consecutive indentations was 150 μm in order to avoid any interference between the individual measurements. Each hardness mapping had at least 300 points of hardness measurements.

3. Experimental results

3.1. Microstructural characteristics

The HPT samples were cut into cross-sections and observed via optical microscopy to examine the stacked layers of Nb and Cu after torsional straining through different numbers of turns (Fig. 2). As expected, the 0.25 turns condition showed almost no change in the Nb layer. It is evident that in the 5 turns condition the Nb layer remains as a continuous layer without becoming disconnected. However, above 10 turns of torsion there is a disconnection in the Nb layer which helps in mixing it into the Cu. The mixture of Nb and Cu has effectively happened at the disk edge after 50 turns while the Cu-Nb interface remains visible at the center part of the disk. Flow stress simulations have also revealed the high strain rate applied to the side of the HPT disk while the centre is lacking any strain rate [37,43,44]. This is due to the centripetal acceleration as explained in Eq. 1 where a_c is the acceleration applied to an object moving in a circle at a linear velocity of v and r is the distance from the center of the circle to a specific point in the circle [45,46]:

$$a_c = \frac{v^2}{r} \tag{1}$$

Also, the linear velocity is dependent upon the distance of the object from the centre of the circle during rotation as described in Eq. 2 where r is the radius and ω is the angular velocity:

$$v = r\omega \tag{2}$$

In HPT experiments conducted at a constant angular velocity ω, the linear velocity is higher at the disk edge resulting in greater acceleration. It follows from kinematics that acceleration is a change in velocity, either in magnitude or in direction or both. In a uniform circular motion, the direction of the velocity changes constantly, so that there is always an associated acceleration even though the magnitude of the velocity may be constant. Thus, the Nb layer near the edge of the disk will rotate with a faster velocity and more acceleration and this produces a better mixture with the Cu layers. This facilitates a faster uniformity around the periphery of the disk as can be witnessed visually in the 50 turns condition while in the central region the Nb interface remains visible until 200 turns when the whole cross-section is uniformly mixed.

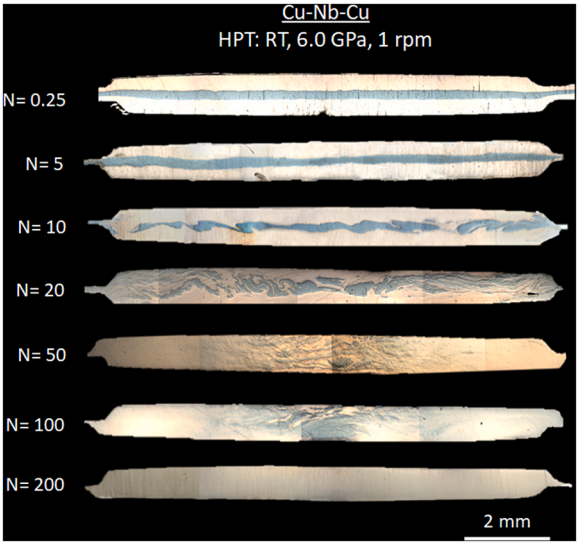

Fig. 2. Optical microscopy of HPT Cu-Nb-Cu layers as a function of number of turns at 6.0 GPa compressive force and 1 rpm torsion.

Electron microscopy images were used to complement the optical microscopy results and compare the inhomogeneity between the 50, 100 and 200 turns samples with the highest torsion numbers at both the center and edge regions (Fig. 3). Due to the difference in atomic number of Cu and Nb, the Z contrast produced in the back scattered electron (BSE) images can reveal a rough estimation of the segregation levels at the macro scale. A comparison between the edge and center of the disk shows that in the early stages of HPT (0.25 and 5 in Fig. 2) a continuous Nb layer continues to hold its position while it starts to break into smaller regions through the thickness after 50. At the electron microscopic level, the Nb-rich layers (bright regions in Fig. 3) gradually disappear and break into smaller areas until a uniform microstructure is obtained at 200 turns. A similar trend was observed earlier where a uniform microstructure was obtained after 150 turns of HPT in a Cu-Ta alloy [26]. By comparing the center and edge of the disks after 50, 100 and 200 turns, it is observed that the homogeneity of mechanical alloying takes place effectively at the edge initially (Figs. 3b, 3d, 3f) and later moves towards the center (Figs. 3a, 3c, 3e). At the initial stage of HPT, the Nb-rich areas appear to form turbulent flow patterns (Figs. 3a, 3c). Similar observations were reported in the flow patterns formed during HPT of various metals where it was shown that vortex-like instabilities can form on the metal layers driven by SPD and local shearing [47–50]. Composition analysis will be further discussed in the red square regions of Figs. 3a, 3c and 3e in Fig. 6.

For evaluation of the chemical composition homogeneity in the 200 HPT sample, more detailed analysis was performed using SEM equipped with an EDS detector to reveal the chemical composition variations within the microscale of the specimen (Fig. 4 and Fig. 5). According to the back-scattered electron (BSE) images taken from the center (Fig. 4) and the edge of the circular disk (Fig. 5), the Z-contrast between the Nb and Cu reveals flow patterns during the test including layers of Cu-Nb segregations in Fig. 4a. At the center, EDS mapping of Cu and Nb in Fig. 4b locates the depletion and enrichment of the Cu and Nb phases. Considering the line scanning data taken from a selected location from each region, the widths of the segregation layers can be estimated as ~3 μm. On the other hand, at the edge of the 200 turns disk almost all segregations have been eliminated and a uniform Cu-20 at% Nb solid solution is formed. Knowing that the solubility of Nb into Cu at room temperature is almost negligible under equilibrium conditions, these results clearly demonstrate the effectiveness of the HPT processing on the supersaturation of Nb into Cu far away from the standard equilibrium condition and specifically at the edge of the 200 turns disk. As shown in the BSE images of Fig. 4 and Fig. 5 from the 200 turns condition, the HPT has effectively led to severe plastic deformation in both the Cu-rich and Nb-rich phases. Nevertheless, the grain structure is not visible using the scanning electron microscopy technique.

To compare the effectiveness of mechanical alloying in forcing Nb atoms into the Cu crystal lattice quantitatively, an EDS line scan was taken from the center of the HPT specimens at the 50, 100 and 200 conditions as presented in Fig. 6. When comparing Figs. 6a, 6b and 6c together, it is apparent that there is an increase in the solid solutioning of Nb into the Cu phase and vice versa. From the EDS line scan data, it was measured that the content of Nb substituted into Cu increased from ~ 4.91 ± 2.8 at% Nb to ~ 11.7 ± 3 at% Nb and ~ 18 ± 2.7 at% Nb in the 50, 100 and 200 HPT turns specimens, respectively. Additionally, the thickness of the Cu/Nb segregation was reduced by increasing the numbers of torsional turns.

Further to confirm the formation of the solid solution of Cu-Nb after HPT processing, XRD was taken from the cross-sections of all samples

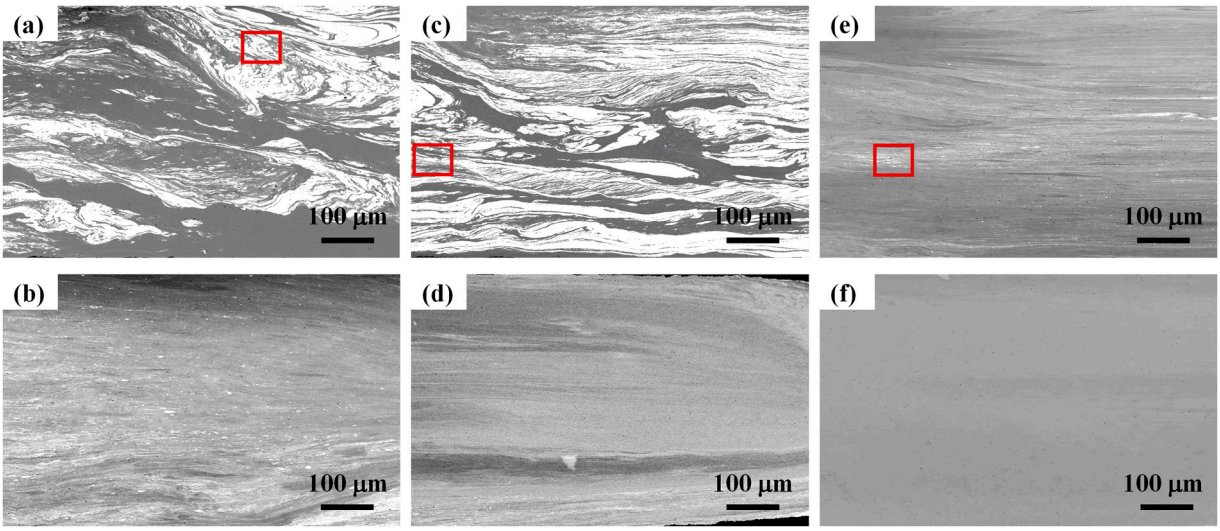

Fig. 3. SEM BSE images taken from a, b) 50, c, d) 100, and e, f) 200 turns at a, c, e) centre and b, d, f) corner of the disk cross-section. Red square regions of Figs. 3a, 3c, and 3e are magnified in Figs. 6a, 6b, and 6c for further microstructural and compositional analysis.

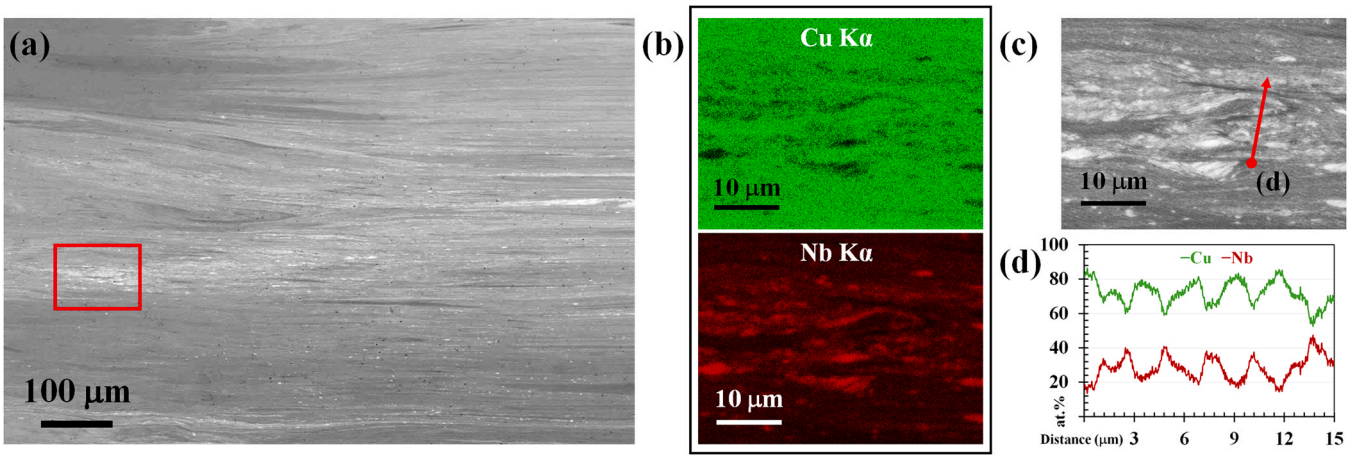

Fig. 4. a) BSE image at the centre of the 200 turns condition with EDS b) Cu Kα & Nb Kα taken from c) high magnification BSE image area from the red square shown in (a) accompanied by d) selected line scan data of Cu and Nb in at% shown in (c).

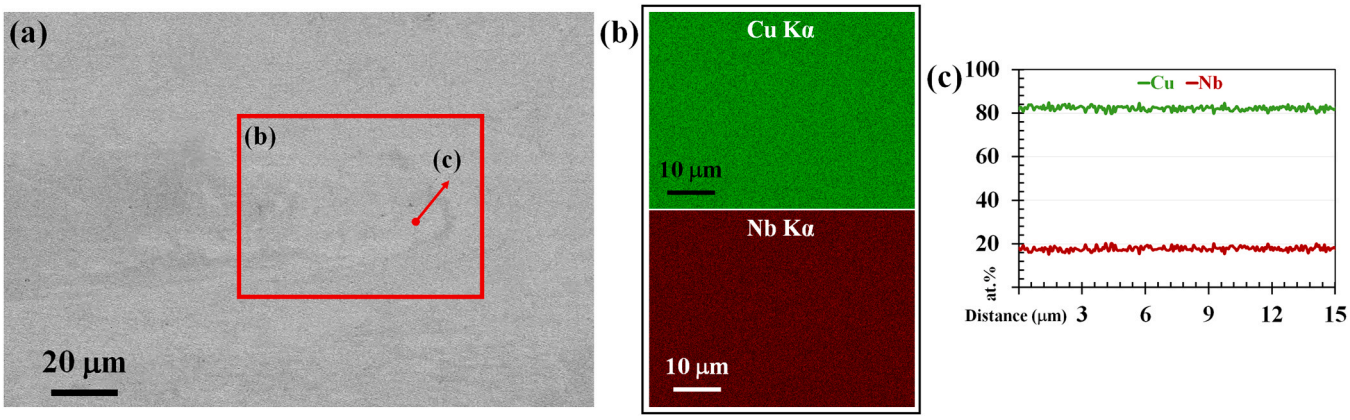

Fig. 5. a) BSE image at the corner of 200 turns condition with EDS b) Cu Kα, Nb Kα taken from the red square shown in (a) accompanied by c) selected line scan data of Cu and Nb in at% shown in (a).

after 0.25, 5, 10, 20, 50, 100 and 200 turns as depicted in Fig. 7. The XRD data were then fitted using Lorentzian fitting to eliminate the background and only the Cu peaks were considered for analysis. A careful examination of the Cu peaks reveals a systematic decrease in their relative intensities and noticeable peak broadening as the number of HPT turns increases. This broadening is attributed to the refinement

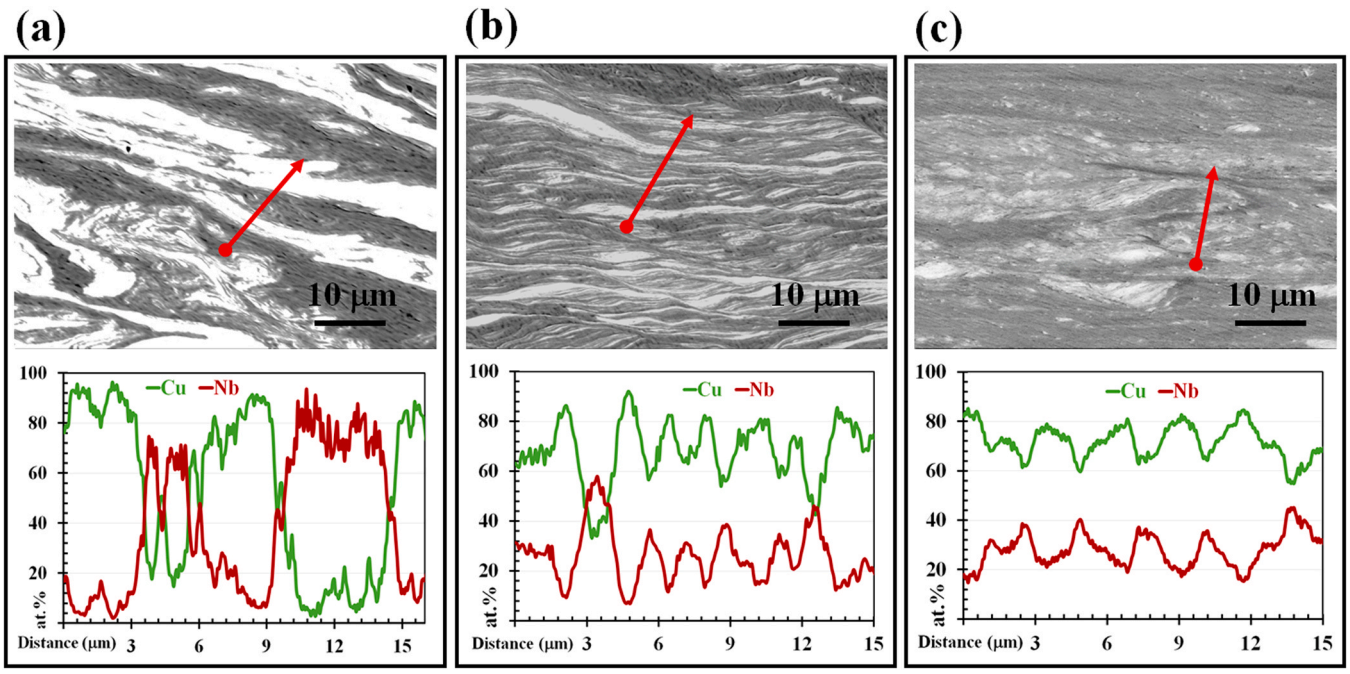

Fig. 6. BSE images of the HPT samples at a) 50, b) 100 and c) 200 turn conditions accompanied by the corresponding quantitative atomic percent line scanning from red lines shown in BSE images.

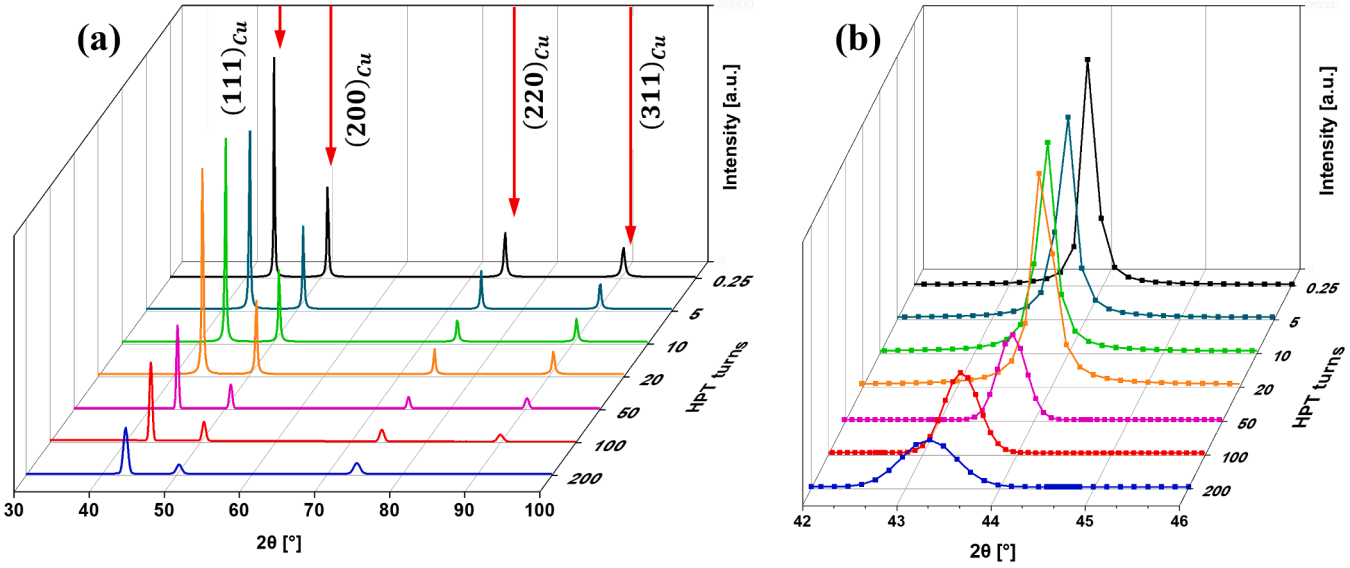

Fig. 7. a) XRD pattern on Cu-Nb HPT specimens after 0.25, 5, 10, 20, 50, 100 and 200 turns and b) magnified XRD pattern at $(111)_{Cu}$ peak.

of crystallite size and the corresponding increase in internal strain (Fig. 7b). Additionally, the inability to recrystallize at room temperature in the samples leads to a reduction of grain size to the sub-micrometer range.

Thus, the crystallite size and lattice distortion, which is representative of the residual strain, were calculated according to the Williamson-Hall method [51] which provides a straightforward approach to analyzing XRD peak broadening by considering both crystallite size and lattice strain effects. According to this method, the total broadening (B_{total}) of an XRD peak obtained by measuring the width of the XRD peak at an intensity equal to the full width half maximum (FWHM) arises from two primary contributions: size broadening ($B_{crystallite}$) and lattice strain broadening (B_{strain}). The values of $B_{crystallite}$ and B_{strain} can be obtained from Eq. 3 and Eq. 4, respectively:

$$B_{crystallite} = \frac{K\lambda}{L\cos\theta} \tag{3}$$

and

$$B_{strain} = C_\varepsilon \tan\theta \tag{4}$$

where λ is the wavelength of the monochromatic X-ray used, θ is the Bragg angle, L is the average crystallite size, K is a shape constant equal to 0.90 and C_ε is micro strain in the material. By combining Eq. 3 and Eq. 4, the Williamson-Hall equation is then expressed as

$$B_{total}\cos\theta = \frac{K\lambda}{L} + 4 \quad C_\varepsilon \sin\theta \tag{5}$$

Plotting $B_{total}\cos\theta$ against $4\sin\theta$ yields a linear relationship, where the intercept provides an estimate of the crystallite size (L), and the slope corresponds to the microstrain (C_ε). This method allows for a more comprehensive evaluation of microstructural changes in materials subjected to SPD processing such as HPT.

The calculated data were then plotted according to the numbers of turns in Fig. 8 where it shows a trend of increasing lattice strain as a result of cold working as well as inducing Nb atoms into the Cu lattice and vice versa. Such a reduction of crystallite size down to the nanoscale regions was also reported in some pure metals and alloys [26,52].

According to Fig. 7, the peak shifting of Cu towards the left (lower angles) by increasing numbers of turns indicates an increase in the lattice parameter of Cu due to the dissolution of Nb atoms in the crystal structure that confirms the Cu-Nb solid solution formation. Since the size of the Nb atoms is larger than Cu, the insertion of Nb into the Cu-FCC structure leads to an enhancement of the crystal lattice and hence a reduction in the 2θ angle in the Bragg diffraction. The mean lattice parameter of the Cu in the metastable Cu-Nb alloy was computed by Materials Analysis Using Diffraction (MAUD) [53] using XRD data. The lattice parameter of Cu was calculated to be approximately 0.358 nm for 0.25, 5, 10 and 20 turns, while after 50, 100 and 200 turns the lattice parameter was calculated as 0.359, 0.361 and 0.363 nm, respectively. Since with increasing numbers of HPT turns over 50 the lattice parameter of Cu increases, it is additional evidence showing the insertion of Nb atoms in the Cu lattice and the formation of a solid solution of the Cu-Nb alloy. These changes in lattice parameter align with findings from similar studies, where the formation of a Cu-Nb solid solution resulted in an expanded Cu lattice parameter [54]. The pure Cu and pure Nb lattice parameters are 0.358 nm [55] and 0.334 nm [56], respectively. Considering the calculated mean lattice parameter of the metastable Cu-Nb alloy and Vegard's law (Eq. 6) [57], the average concentration of Nb in Cu within the entire disc processed at 50, 100 and 200 turns achieved ~ 4.2 ± 0.1 at% Nb, ~ 12.5 ± 0.02 at% Nb, and ~ 17 ± 0.02 at% Nb, respectively. It is noted that, consistent with the EDX data, these values are remarkably high when using a processing route involving a bulk-state reaction without the application of an elevated processing temperature. Thus,

$$a_{A_{1-x}B_x} = (1-x)a_A + x \quad a_B \tag{6}$$

where $a_{A_{1-x}B_x}$ is the lattice parameter of the solid solution, a_A and a_B are the lattice parameters of the pure constituents (here Cu and Nb) and x is the molar fraction of constituent B in which, if multiplied to 100, it is equivalent to the atomic percentage of constituent B in the solid solution.

Fig. 9a shows a high magnification transmission electron microscopy (TEM) image from the center of the disc processed through 200 turns. The Nb-rich regions are in dark color and it is obvious that the microstructure consists of a matrix of a Cu-rich Cu-Nb alloy with secondary Nb-rich regions distributed uniformly throughout the matrix. Overall, the Nb-rich regions are well distributed over the matrix but their size and shape are different. Fig. 9b shows a high magnification TEM image from a selected area in Fig. 9a which demonstrates that the Cu-rich matrix contains very fine crystallites of the order of ~5–10 nm. The interface between these Nb-rich regions and the Cu-rich matrix exhibits strong atomic bonding, with no detectable porosity or cracks because of any enhanced diffusion occurring between the Cu and Nb through the HPT processing.

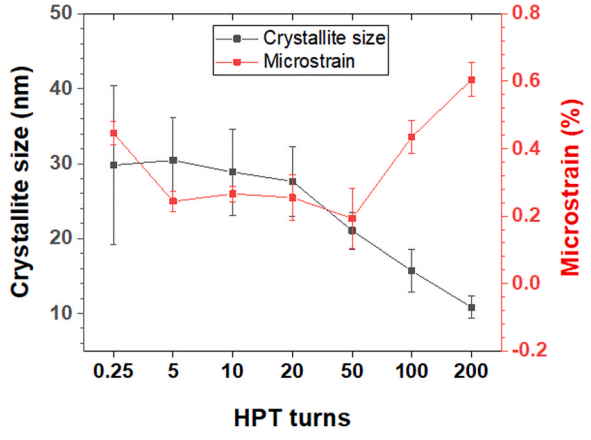

Fig. 8. Calculated crystallite size and lattice strain in Cu after various HPT turns.

3.2. Mechanical properties

Initial inspection of the mechanical properties was performed by hardness mapping and the mapping after 0.25, 10, 50, 100 and 200 turns is depicted in Fig. 10 at a constant color scale of 0 – 350 Hv. The distinction between the hard Nb plate and the soft Cu plate is clearly visible in the first three samples having low numbers of turns (for $N = 0.25$, 5 and 10 turns conditions) in Figs. 10a-10c which is an indication of the heterogeneity after HPT in the early stages. Nevertheless, the plastic deformation and work-hardening at room temperature as a result of SPD is sufficient to boost the hardness of the Cu disk to an average of ~100 ~ 150 Hv which is relatively higher than the annealed state [42]. On the other hand, the second group consisting of samples with a higher number of 50 and 100 turns demonstrates a significant boost in hardness where the centerline Nb disappears and a uniform hardness value of about 350 Hv exists throughout the sample thickness at the sample edge while an inhomogeneity in hardness is apparent at the centre of the disks as shown in Fig. `10d and 10e. This is linked to the lack of driving force for mixing. As discussed earlier, the lower linear velocity during rotation at smaller r values (i.e. the distance from the centre of the disk) does not provide a sufficient driving force for mechanical alloying and hence requires more rotation for complete homogeneity. After 200 turns, however, a homogenous hardness value across the whole thickness and width of the disk cross-section was obtained (Fig. 10f) and this confirms the effectiveness of using HPT in the homogenization of the non-equilibrium Cu-Nb alloy system and producing high-strength materials without requiring any high temperature processing routes such as solidification or forging. Similar demonstrations were given earlier by producing homogeneity in the hardness values of the AA7xxx series [58] and the Cu-0.1 wt%Zr alloy [59] after 10 turns of HPT, whereas in the Cu-Ta alloy there was a homogeneous hardness value of ~350 Hv across the HPT sample after 150 turns [26]. This research found that complete homogeneity was obtained after 200 turns in the Cu-Nb alloy system.

To evaluate the mechanical properties of the HPT specimens, the engineering stress-strain curves of the miniature tensile specimens at 1.0×10^{-3} s^{-1} strain rate are shown in Fig. 11. Due to the uneven composition of the HPT specimen after lower numbers of turns, only the 200 turns sample was targeted for tensile properties as it showed a uniform chemical composition throughout the disk. An initial comparison between the tensile properties with that of HPT pure Cu [60] confirms the effectiveness of the HPT mechanical alloying of Cu in boosting the mechanical properties to ~1250 MPa with a reasonable elongation of ~ 40 %. Considering the high-volume Cu and less Nb in this newly fabricated Cu-Nb composite, this is a novel strategy to design Cu-based bi-metallic composites for achieving high mechanical strength.

After applying the post-HPT annealing heat treatment, the yield strength decreased to ~1000 and ~700 MPa by increasing the annealing temperature from 973 K to 1173 K (Fig. 11) which is a sign of recovery and recrystallization of Cu at these high temperatures. It should be noted that the yielding point and peak stress position are very close in the engineering stress-strain curves which leads to the material having limited uniform elongation. This is due to an extremely saturated high

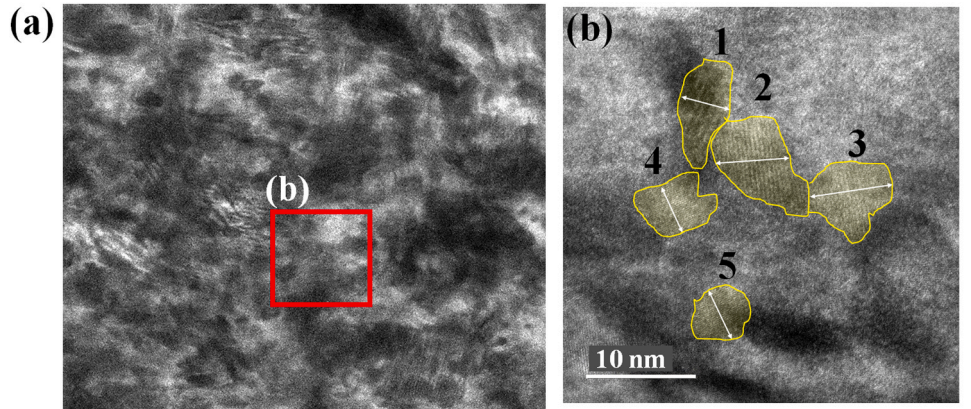

Crystallite number	1	2	3	4	5
Size (nm)	~ 4.7	~ 5.8	~ 9	~ 4.8	~ 5.5

Fig. 9. a) TEM image of the Cu-Nb from the center of the disc after 200 HPT turns, b) high magnification image of the Nb-rich regions and the Cu-rich matrix. Cu-rich crystallites are enveloped in yellow, and their size are presented in the table below the image.

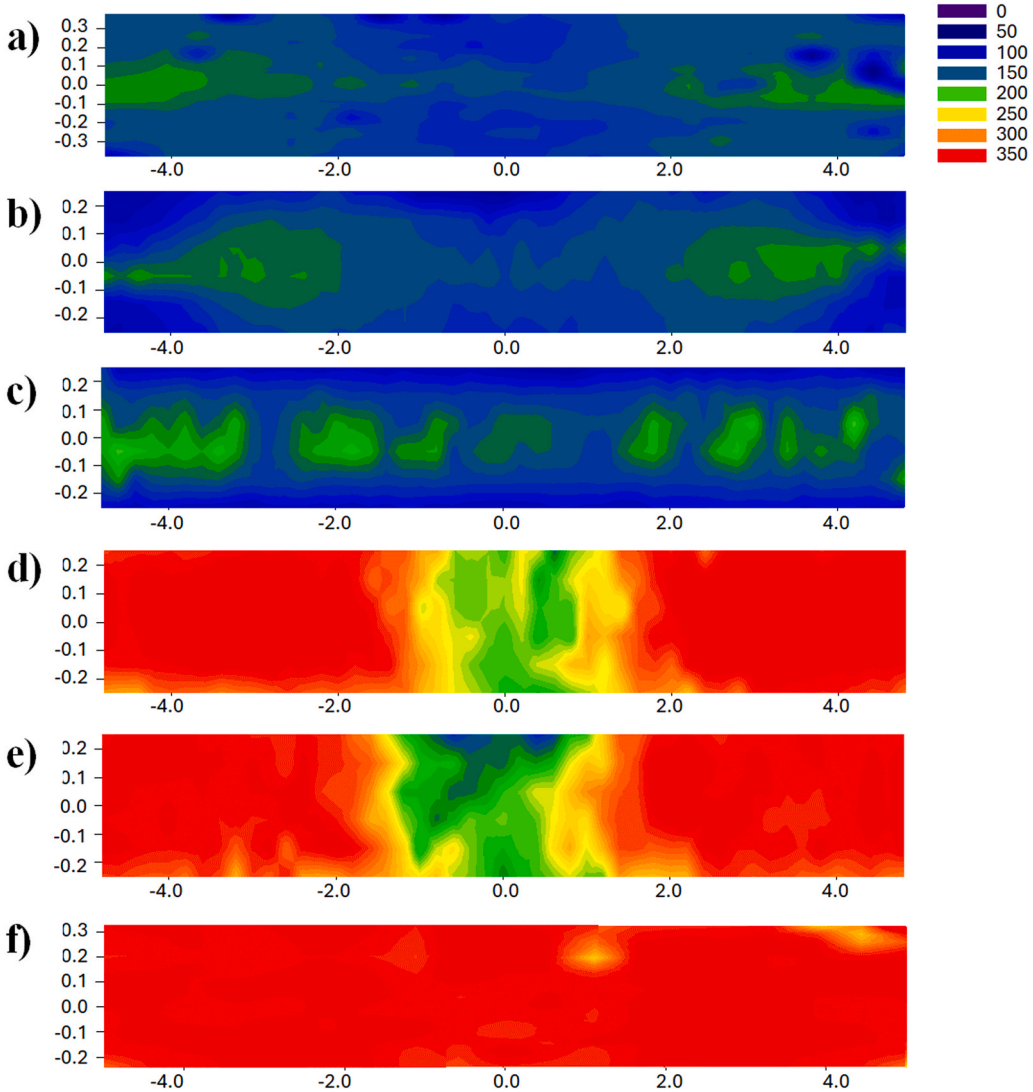

Fig. 10. Hardness mapping of samples after N number of turns a) 0.25, b) 5, c) 10, d) 50, e) 100 and f) 200. Dimensions are in millimeters.

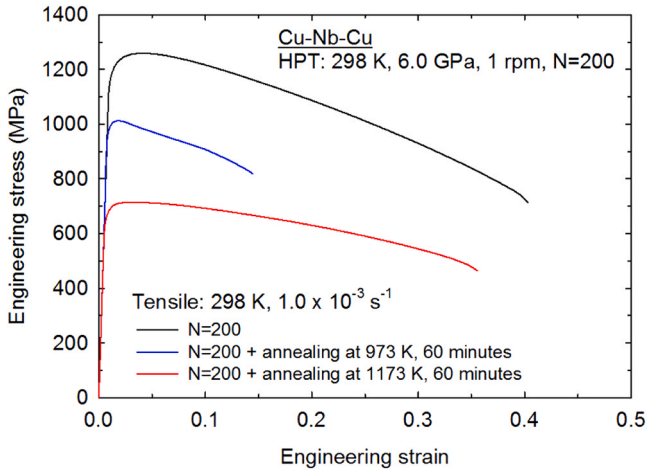

Fig. 11. Engineering stress-strain curve of the Cu-Nb-Cu subsize tensile specimen after 200 turns HPT compared with annealing using two different heat treatments.

density of dislocations in the microstructure.

To justify the effect of the annealing heat treatment on the mechanical properties of the HPT 200 turns sample, microstructural analysis using SEM-EDS was performed on samples after the 973 K and 1173 K annealing heat treatments presented in Fig. 12. By comparing the BSE image of Fig. 12a taken at the centre of the specimen cross-section with Fig. 4a, some bright areas enriched in Nb are observed. By taking EDS mapping of Cu and Nb (Fig. 12b) and a selected line scan profile (Fig. 12c) and comparing with Fig. 4e, it is possible to identify segregation of Nb out of the Cu matrix resulting in an increasing Nb to Cu ratio by thermal annealing. This is due to the extremely low solubility limit of Nb into Cu in the equilibrium condition which is provided through the thermal annealing. The same phenomenon also takes place after the 1173 K annealing heat treatment according to Fig. 12f.

4. Discussion

The microstructural evolution and phase transformation in the Cu-Nb sample during HPT shows a progressive refinement process. Initially, the Nb layers undergo thinning due to the applied shear strain, gradually breaking into small Nb-rich layers. As the HPT process continues, these layers become finer and disperse uniformly within the Cu matrix (Figs. 3 and 6). Since strain distribution is higher at the disc edge, microstructural refinement begins from the edge and progresses towards the centre with increasing HPT turns (Figs. 2 and 3). At higher strain levels (200 turns), the entire sample transforms into a homogeneous Cu-Nb alloy, demonstrating the effectiveness of HPT in achieving atomic-scale mixing and enhanced solubility.

With increasing HPT turns, the applied strain leads to further grain refinement in the Cu-Nb system, introducing more crystalline defects and generating new diffusion pathways for the Cu and Nb atoms. XRD analysis suggests that substantial atomic diffusion occurs after approximately 50 HPT turns. The crystallite sizes of Cu at 50, 100 and 200 turns are around 20, 15 and 10 nm, representing size reductions of ~30 %, ~46 % and ~65 %, respectively. These reductions increase the fractions of grain boundaries which serve as effective diffusion paths. It can therefore be concluded that after approximately 50 HPT turns, the increased number of grain boundaries and crystalline defects provide effective diffusion pathways for atoms [61]. As the HPT process continues, the Nb-rich regions become finer as the width of the Nb-rich regions at 50, 100 and 200 turns decreases gradually through ~ 4.5 ± 1.0 μm, ~ 2.2 ± 0.7 μm and ~ 1.2 ± 0.5 μm, respectively, further promoting diffusion between Cu and Nb and facilitating the formation of a solid solution (Fig. 6). Moreover, the solid solution formation of Cu-Nb alloy after 200 HPT turns was confirmed through an increase in the lattice parameter of Cu and internal lattice strain through XRD analysis. Therefore, based on the XRD and EDX data, at 200 HPT turns, the solubility of Nb in Cu reaches notably high levels. These findings demonstrate that HPT enables the formation of a metastable Cu-Nb solid solution at room temperature without requiring elevated processing temperatures.

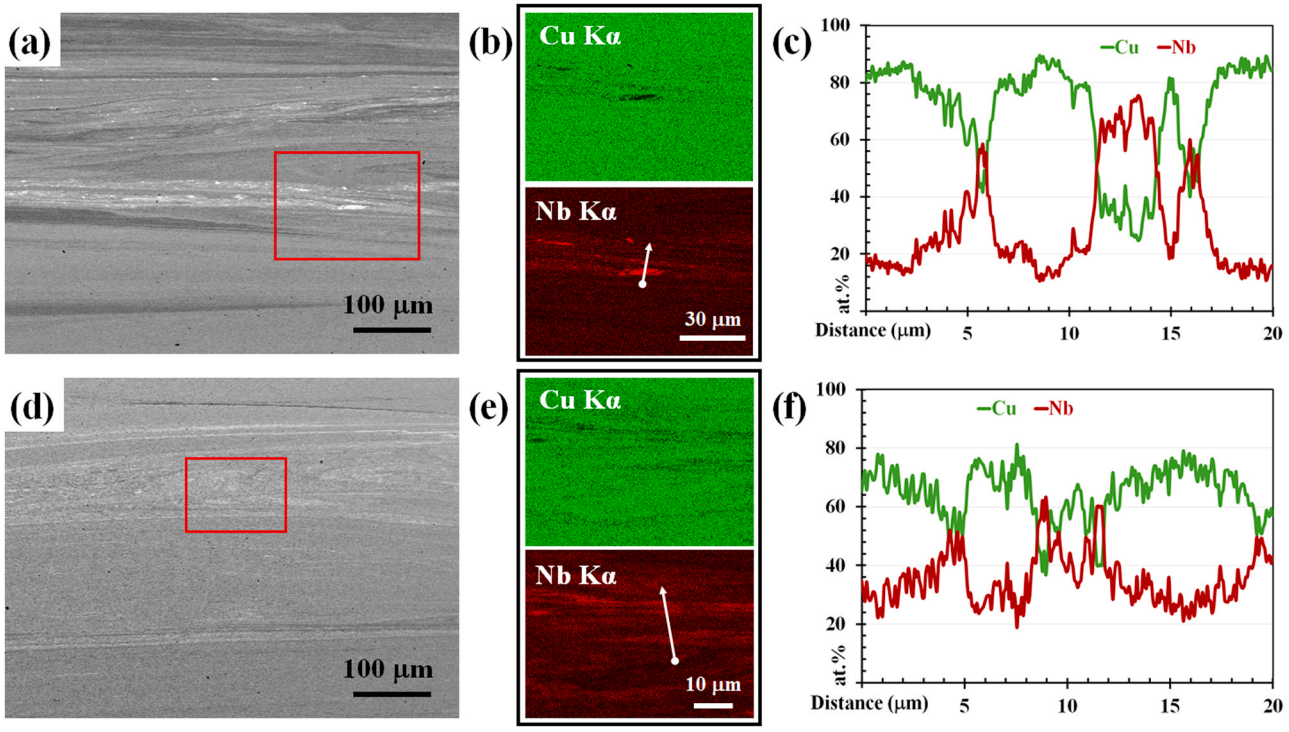

Fig. 12. Microstructure of 200 turns specimen after a, b, c) 973 K and d, e, f) 1173 K presenting BSE image through thickness and selected area EDS b, e) Cu Kα & Nb Kα mapping accompanied by c, f) line scan profile data of Cu and Nb in at%.

After 200 HPT turns, the Cu-Nb alloy exhibited a UTS of ~ 1250 MPa, an elongation of ~ 40 % and a microhardness of ~ 350 Hv. Compared to HPT-processed pure Cu with a UTS of ~ 500 MPa and hardness of ~120 Hv [60], the strength of the HPT-processed Cu-Nb alloy is significantly enhanced. Interestingly, despite having a higher Cu content, the presence of Nb appears to play a major role in strengthening the material.

The strengthening mechanism can be attributed to the refined microstructure. Additionally, the alloy consists of a Cu-rich matrix containing dispersed Nb-rich layers which significantly enhance the mechanical properties. Solid solution strengthening occurs due to the increased lattice parameter of Cu from the dissolution of Nb atoms. Interface strengthening arises from the Nb-rich layers acting as barriers to dislocation movement. Finally, crystallite refinement strengthening results from the severe plastic deformation during HPT, which increases the density of grain boundaries and further contributes to the enhanced mechanical strength.

The elongation of ~ 40 % obtained in the 200 turns HPT-processed Cu-Nb alloy demonstrates a good balance between high strength and reasonable ductility. Typically, increasing strength leads to reduced ductility but the HPT-processed Cu-Nb alloy maintains a relatively high elongation compared to pure HPT-processed Cu after 10 HPT turns (~ 4 %) [62]. The improved ductility of the Cu-Nb alloy is attributed to the interfaces between the Cu-rich matrix and the Nb-rich layers which influence load transfer and dislocation interactions. These interfaces provide strain hardening and improve the ability of the alloy to accommodate plastic deformation thereby resulting in enhanced elongation.

5. Conclusions

The binary immiscible Cu-Nb alloy was investigated using HPT processing by stacking Cu-Nb-Cu layers and processing through different numbers of turns under a 6.0 GPa compressive force to produce mechanically alloyed disks. The microstructural character and the mechanical properties were analyzed leading to the following conclusions.

- The HPT processing produces a bulk disk material of the immiscible Cu-Nb binary alloy homogenized after 200 turns without the presence of any porosity, inclusions or cavities.
- The homogeneity of the torsion samples increases by increasing the number of turns. While homogeneity at the centre of the disks occurs slowly, segregations at the edge are easily removed due to the centripetal acceleration which leads to more applied strain.
- The segregation layers become narrower with smaller fluctuations leading to the formation of a non-equilibrium Cu- ~17 at%Nb solid solution in the entire disc processed at 200 HPT turns.
- Both residual strain and crystallite size are reduced by increasing the number of HPT turns indicating both mechanical cold working as well as an increasing Nb insertion into the Cu crystal structure.
- The mechanical properties show a negative work-hardening behavior in the 200 turns condition with a UTS of over ~ 1250 MPa. Applying the post-HPT annealing heat treatment reduces the tensile strength to ~700 MPa due to increasing Nb segregation.

CRediT authorship contribution statement

Zargar Tahereh: Writing – review & editing, Writing – original draft, Visualization, Investigation, Formal analysis, Data curation. **Sadeghi Fazlollah:** Writing – review & editing, Writing – original draft, Software, Investigation, Data curation. **Mousavi Tayebeh:** Writing – review & editing, Validation, Supervision, Resources, Data curation. **Planat Solène:** Investigation, Formal analysis, Data curation. **Öğüt Serkan:** Investigation, Formal analysis, Data curation. **Huang Yi:** Writing – review & editing, Supervision, Resources, Methodology, Funding acquisition. **Langdon Terence G.:** Writing – review & editing, Supervision, Project administration, Data curation, Conceptualization.

Declaration of Competing Interest

The authors declare that they have no known competing financial interests or personal relationships that could have appeared to influence the work reported in this paper.

References

[1] R.Z. Valiev, R.K. Islamgaliev, I.V. Alexandrov, Bulk nanostructured materials from severe plastic deformation, Prog. Mater. Sci. 45 (2000) 103–189, https://doi.org/10.1016/S0079-6425(99)00007-9.

[2] R.Z. Valiev, Y. Estrin, Z. Horita, T.G. Langdon, M.J. Zehetbauer, Y.T. Zhu, Producing bulk ultrafine-grained materials by severe plastic deformation, JOM 58 (4) (2006) 33–39, https://doi.org/10.1007/s11837-006-0213-7.

[3] K. Edalati, A. Bachmaier, V.A. Beloshenko, Y. Beygelzimer, V.D. Blank, W.J. Botta, K. Bryła, J. Čížek, S. Divinski, N.A. Enikeev, Y. Estrin, G. Faraji, R.B. Figueiredo, M. Fuji, T. Furuta, T. Grosdidier, J. Gubicza, A. Hohenwarter, Z. Horita, J. Huot, Y. Ikoma, M. Janeček, M. Kawasaki, P. Král, S. Kuramoto, T.G. Langdon, D. R. Leiva, V.I. Levitas, A. Mazilkin, M. Mito, H. Miyamoto, T. Nishizaki, R. Pippan, V.V. Popov, E.N. Popova, G. Purcek, O. Renk, Á. Révész, X. Sauvage, V. Sklenicka, W. Skrotzki, B.B. Straumal, S. Suwas, L.S. Toth, N. Tsuji, R.Z. Valiev, G. Wilde, M. J. Zehetbauer, X. Zhu, Nanomaterials by severe plastic deformation: review of historical developments and recent advances, Mater. Res. Lett. 10 (2022) 163–256, https://doi.org/10.1080/21663831.2022.2029779.

[4] K. Edalati, A.Q. Ahmed, S. Akrami, K. Ameyama, V. Aptukov, R.N. Asfandiyarov, M. Ashida, V. Astanin, A. Bachmaier, V. Beloshenko, E.V. Bobruk, K. Bryła, J. M. Cabrera, A.P. Carvalho, N.Q. Chinh, I.C. Choi, R. Chulist, J.M. Cubero-Sesin, G. Davdian, M. Demirtas, S. Divinski, K. Durst, J. Dvorak, P. Edalati, S. Emura, N. A. Enikeev, G. Faraji, R.B. Figueiredo, R. Floriano, M. Fouladvind, D. Fruchart, M. Fuji, H. Fujiwara, M. Gajdics, D. Gheorghe, L. Gondek, J.E. González-Hernández, A. Gornakova, T. Grosdidier, J. Gubicza, D. Gunderov, L. He, O. F. Higuera, S. Hirosawa, A. Hohenwarter, Z. Horita, J. Horky, Y. Huang, J. Huot, Y. Ikoma, T. Ishihara, Y. Ivanisenko, J. il Jang, A.M. Jorge, M. Kawabata-Ota, M. Kawasaki, T. Khelfa, J. Kobayashi, L. Kommel, A. Korneva, P. Kral, N. Kudriashova, S. Kuramoto, T.G. Langdon, D.H. Lee, V.I. Levitas, C. Li, H.W. Li, Y. Li, Z. Li, H.J. Lin, K.D. Liss, Y. Liu, D.M.M. Cardona, K. Matsuda, A. Mazilkin, Y. Mine, H. Miyamoto, S.C. Moon, T. Müller, J.A. Muñoz, M.Y. Murashkin, M. Naeem, M. Novelli, D. Olasz, R. Pippan, V.V. Popov, E.N. Popova, G. Purcek, P. de Rango, O. Renk, D. Retraint, Á. Révész, V. Roche, P. Rodriguez-Calvillo, L. Romero-Resendiz, X. Sauvage, T. Sawaguchi, H. Sena, H. Shahmir, X. Shi, V. Sklenicka, W. Skrotzki, N. Skryabina, F. Staab, B. Straumal, Z. Sun, M. Szczerba, Y. Takizawa, Y. Tang, R.Z. Valiev, A. Vozniak, A. Voznyak, B. Wang, J.T. Wang, G. Wilde, F. Zhang, M. Zhang, P. Zhang, J. Zhou, X. Zhu, Y.T. Zhu, Severe plastic deformation for producing superfunctional ultrafine-grained and heterostructured materials: An interdisciplinary review, J. Alloy. Compd. 1002 (2024), https://doi.org/10.1016/j.jallcom.2024.174667.

[5] R.Z. Valiev, O.A. Kaibyshev, R.I. Kuznetsov, R.Sh Musalimov, N.K. Tsenev, Low-temperature superplasticity of metallic materials, Dokl. Akad. Nauk SSSR 301 (1988) 864–866.

[6] V.M. Segal, V.I. Reznikov, A.E. Drobyshevsky, I. Kopylov, Plastic metal working by simple shear, Russ. Met. 1 (1981) 115–123.

[7] R.Z. Valiev, T.G. Langdon, principles of equal-channel angular pressing as a processing tool for grain refinement, Prog. Mater. Sci. 51 (2006) 881–981, https://doi.org/10.1016/j.pmatsci.2006.02.003.

[8] Y. Saito, N. Tsuji, H. Utsunomiya, T. Sakai, R.G. Hong, Ultra-fine grained bulk aluminum produced by accumulative roll-bonding (ARB) process, Scr. Mater. 39 (1998) 1221–1227, https://doi.org/10.1016/S1359-6462(98)00302-9.

[9] Y. Saito, H. Utsunomiya, N. Tsuji, T. Sakai, Novel ultra-high straining process for bulk materials – development of the accumulative roll-bonding (ARB) process, Acta Mater. 47 (1999) 579–583, https://doi.org/10.1016/S1359-6454(98)00365-6.

[10] N. Tsuji, Y. Saito, H. Utsunomiya, S. Tanigawa, Ultra-fine grained bulk steel produced by accumulative roll-bonding (ARB) process, Scr. Mater. 40 (1999) 795–800, https://doi.org/10.1016/S1359-6462(99)00015-9.

[11] S.M. Ghalehbandi, M. Malaki, M. Gupta, Accumulative roll bonding – a review, 1-32, Appl. Sci. 9 (2019) 3627, https://doi.org/10.3390/app9173627.

[12] P.W. Bridgman, Effect of high shearing stress combined with high hydrostatic pressure, Phys. Rev. 48 (1935) 825–847, https://doi.org/10.1103/PhysRev.48.825.

[13] P.W. Bridgman, On torsion combined with compression, J. Appl. Phys. 14 (1943) 273–283, https://doi.org/10.1063/1.1714987.

[14] D.I. Tupitsa, V.P. Pilyugin, R.I. Kuznetsov, G.G. Taluts, V.A. Teplov, Deformation-induced transitions in Kh29N8 alloy under high pressure, Fiz. Metal. Met. 61 (2) (1986) 325–330.

[15] A.P. Zhilyaev, T.G. Langdon, Using high-pressure torsion for metal processing: fundamentals and applications, Prog. Mater. Sci. 53 (2008) 893–979, https://doi.org/10.1016/j.pmatsci.2008.03.002.

[16] J.K. Han, J.I. Jang, T.G. Langdon, M. Kawasaki, Bulk-state reactions and improving the mechanical properties of metals through high-pressure torsion, Mater. Trans. 60 (2019) 1131–1138, https://doi.org/10.2320/matertrans.MF201908.

[17] D. Hernández-Escobar, M. Kawasaki, C.J. Boehlert, Metal hybrids processed by high-pressure torsion: synthesis, microstructure, mechanical properties and developing trends, Int. Mater. Rev. 67 (2022) 231–265, https://doi.org/10.1080/09506608.2021.1922807.
[18] K. Oh-Ishi, K. Edalati, H.S. Kim, K. Hono, Z. Horita, High-pressure torsion for enhanced atomic diffusion and promoting solid-state reactions in the aluminum-copper system, Acta Mater. 61 (2013) 3482–3489, https://doi.org/10.1016/j.actamat.2013.02.042.
[19] O. Bouaziz, H.S. Kim, Y. Estrin, Architecturing of metal-based composites with concurrent nanostructuring: A new paradigm of materials design, Adv. Eng. Mater. 15 (2013) 336–340, https://doi.org/10.1002/adem.201200261.
[20] B. Ahn, A.P. Zhilyaev, H.J. Lee, M. Kawasaki, T.G. Langdon, Rapid synthesis of an extra hard metal matrix nanocomposite at ambient temperature, Mater. Sci. Eng. A 635 (2015) 109–117, https://doi.org/10.1016/j.msea.2015.03.042.
[21] S.A. Nikulin, S.O. Rogachev, A.B. Rozhnov, V.M. Khatkevich, T.A. Nechaikina, M. V. Morozov, Structure and properties of a layered steel/vanadium alloy/steel composite prepared by high-pressure torsion, Russ. Met. 2016 (2016) 375–379, https://doi.org/10.1134/S0036029516040169.
[22] M. Kawasaki, B. Ahn, H. Lee, A.P. Zhilyaev, T.G. Langdon, Using high-pressure torsion to process an aluminum-magnesium nanocomposite through diffusion bonding, J. Mater. Res 31 (2016) 88–99, https://doi.org/10.1557/jmr.2015.257.
[23] V.N. Danilenko, S.N. Sergeev, J.A. Baimova, G.F. Korznikova, K.S. Nazarov, R. K. Khisamov, A.M. Glezer, R.R. Mulyukov, An approach for fabrication of Al-Cu composite by high pressure torsion, Mater. Lett. 236 (2019) 51–55, https://doi.org/10.1016/j.matlet.2018.09.158.
[24] N. Ibrahim, M. Peterlechner, F. Emeis, M. Wegner, S.V. Divinski, G. Wilde, Mechanical alloying via high-pressure torsion of the immiscible Cu50Ta50 system, Mater. Sci. Eng. A 685 (2017) 19–30, https://doi.org/10.1016/j.msea.2016.12.106.
[25] J.K. Han, D.K. Han, G.Y. Liang, J. Il Jang, T.G. Langdon, M. Kawasaki, Direct Bonding of Aluminum–Copper Metals through High-Pressure Torsion Processing, Adv. Eng. Mater. 20 (2018) 1–9, https://doi.org/10.1002/adem.201800642.
[26] T. Mousavi, J. Dai, P. Bazarnik, P.H.R. Pereira, Y. Huang, M. Lewandowska, T. G. Langdon, Fabrication and characterization of nanostructured immiscible Cu–Ta alloys processed by high-pressure torsion, J. Alloy. Compd. 832 (2020) 155007, https://doi.org/10.1016/j.jallcom.2020.155007.
[27] Y.Z. Tian, X.H. An, S.D. Wu, Z.F. Zhang, R.B. Figueiredo, N. Gao, T.G. Langdon, Direct observations of microstructural evolution in a two-phase Cu-Ag alloy processed by high-pressure torsion, Scr. Mater. 63 (2010) 65–68, https://doi.org/10.1016/j.scriptamat.2010.03.014.
[28] E. Botcharova, J. Freudenberger, L. Schultz, Cu-Nb alloys prepared by mechanical alloying and subsequent heat treatment, J. Alloy. Compd. 365 (2004) 157–163, https://doi.org/10.1016/S0925-8388(03)00634-0.
[29] R.S. Lei, M.P. Wang, Z. Li, H.G. Wei, W.C. Yang, Y.L. Jia, S. Gong, Structure evolution and solid solubility extension of copper-niobium powders during mechanical alloying, Mater. Sci. Eng. A. 528 (2011) 4475–4481, https://doi.org/10.1016/j.msea.2011.02.083.
[30] R. Lei, M. Wang, H. Wang, S. Xu, New insights on the formation of supersaturated Cu-Nb solid solution prepared by mechanical alloying, Mater. Charact. 118 (2016) 324–331, https://doi.org/10.1016/j.matchar.2016.06.013.
[31] M.A. Morris, D.G. Morris, Microstructural refinement and associated strength of copper alloys obtained by mechanical alloying, Mater. Sci. Eng. A 111 (1989) 115–127, https://doi.org/10.1016/0921-5093(89)90204-9.
[32] A. Benghalem, D.G. Morris, Microstructure and mechanical properties of concentrated copperniobium alloys prepared by mechanical alloying, Mater. Sci. Eng. A. 161 (1993) 255–266, https://doi.org/10.1016/0921-5093(93)90520-O.
[33] B. Gwalani, Q. Pang, A. Yu, W. Fu, L. Li, M. Pole, C. Roach, S.N. Mathaudhu, T. Ajantiwalay, M. Efe, S. Hu, M. Song, A. Soulami, A. Rohatgi, Y. Li, P.V. Sushko, A. Devaraj, Extended Shear Deformation of the Immiscible Cu-Nb Alloy Resulting in Nanostructuring and Oxygen Ingress with Enhancement in Mechanical Properties, ACS Omega 7 (2022) 13721–13736, https://doi.org/10.1021/acsomega.1c07368.
[34] E. Botcharova, J. Freudenberger, L. Schultz, Mechanical and electrical properties of mechanically alloyed nanocrystalline Cu-Nb alloys, Acta Mater. 54 (2006) 3333–3341, https://doi.org/10.1016/j.actamat.2006.03.021.
[35] A. Inoue, H.M. Kimura, K. Matsuki, T. Masumoto, Preparation of new amorphous Cu-Nb-Sn alloys by mechanical alloying of elemental copper, niobium and tin powders, J. Mater. Sci. Lett. 6 (1987) 979–981, https://doi.org/10.1007/BF01729890.
[36] J. Freudenberger, E. Botcharova, L. Schultz, Formation of the microstructure in Cu-Nb alloys, J. Mater. Sci. 39 (2004) 5343–5345, https://doi.org/10.1023/B:JMSC.0000039241.01005.c6.
[37] M. Kapoor, T. Kaub, K.A. Darling, B.L. Boyce, G.B. Thompson, An atom probe study on Nb solute partitioning and nanocrystalline grain stabilization in mechanically alloyed Cu-Nb, Acta Mater. 126 (2017) 564–575, https://doi.org/10.1016/j.actamat.2016.12.057.
[38] R.B. Figueiredo, P.R. Cetlin, T.G. Langdon, Using finite element modeling to examine the flow processes in quasi-constrained high-pressure torsion, Mater. Sci. Eng. A 528 (2011) 8198–8204, https://doi.org/10.1016/j.msea.2011.07.040.
[39] K. Edalati, Z. Horita, T.G. Langdon, The significance of slippage in processing by high-pressure torsion, Scr. Mater. 60 (2009) 9–12, https://doi.org/10.1016/j.scriptamat.2008.08.042.
[40] K. Edalati, R. Miresmaeili, Z. Horita, H. Kanayama, R. Pippan, Significance of temperature increase in processing by high-pressure torsion, Mater. Sci. Eng. A. 528 (2011) 7301–7305, https://doi.org/10.1016/j.msea.2011.06.031.
[41] P.H.R. Pereira, R.B. Figueiredo, Y. Huang, P.R. Cetlin, T.G. Langdon, Modeling the temperature rise in high-pressure torsion, Mater. Sci. Eng. A. 593 (2014) 185–188, https://doi.org/10.1016/j.msea.2013.11.015.
[42] K. Edalati, Y. Hashiguchi, P.H.R. Pereira, Z. Horita, T.G. Langdon, Effect of temperature rise on microstructural evolution during high-pressure torsion, Mater. Sci. Eng. A. 714 (2018) 167–171, https://doi.org/10.1016/j.msea.2017.12.095.
[43] C. Suryanarayana, M.G. Norton, in: C. Suryanarayana, M.G. Norton (Eds.), Determination of Crystallite Size and Lattice Strain BT - X-Ray Diffraction: A Practical Approach, Springer, US, Boston, MA, 1998, pp. 207–221, https://doi.org/10.1007/978-1-4899-0148-4_9.
[44] R.B. Figueiredo, G.C.V. De Faria, P.R. Cetlin, T.G. Langdon, Three-dimensional analysis of plastic flow during high-pressure torsion, J. Mater. Sci. 48 (2013) 4524–4532, https://doi.org/10.1007/s10853-012-6979-9.
[45] R. Paine, C. Beards, P. Tucker, D.H. Bacon, in: E.H.B.T.-M.E.R.B. Twelfth, E. Smith (Eds.), 1 - Mechanical engineering principles, Butterworth-Heinemann, 1994, pp. 1–48, https://doi.org/10.1016/B978-0-7506-1195-4.50005-1.
[46] M. Blundell, D. Harty, in: M. Blundell, D.B.T.-T.M.S.A. to V.D. (Second E. Harty (Eds.), Chapter 2 - Kinematics and Dynamics of Rigid Bodies, Butterworth-Heinemann, Oxford, 2015, pp. 27–86, https://doi.org/10.1016/B978-0-08-099425-3.00002-9.
[47] R. Kulagin, Y. Beygelzimer, Y. Ivanisenko, A. Mazilkin, B. Straumal, H. Hahn, Instabilities of interfaces between dissimilar metals induced by high pressure torsion, Mater. Lett. 222 (2018) 172–175, https://doi.org/10.1016/j.matlet.2018.03.200.
[48] Y. Cao, M. Kawasaki, Y.B. Wang, S.N. Alhajeri, X.Z. Liao, W.L. Zheng, S.P. Ringer, Y.T. Zhu, T.G. Langdon, Unusual macroscopic shearing patterns observed in metals processed by high-pressure torsion, J. Mater. Sci. 45 (2010) 4545–4553, https://doi.org/10.1007/s10853-010-4485-5.
[49] Y. Huang, M. Kawasaki, T.G. Langdon, Influence of anvil alignment on shearing patterns in high-pressure torsion, Adv. Eng. Mater. 15 (2013) 747–755.
[50] Y. Huang, M. Kawasaki, T.G. Langdon, An evaluation of the shearing patterns introduced by different anvil alignments in high-pressure torsion, J. Mater. Sci. 49 (2014) 3146–3157.
[51] G.K. Williamson, W.H. Hall, X-ray line broadening from filed aluminium and wolfram, Acta Met. 1 (1953) 22–31.
[52] A.P. Zhilyaev, G.V. Nurislamova, B.K. Kim, M.D. Baró, J.A. Szpunar, T.G. Langdon, Experimental parameters influencing grain refinement and microstructural evolution during high-pressure torsion, Acta Mater. 51 (2003) 753–765, https://doi.org/10.1016/S1359-6454(02)00466-4.
[53] L. Lutterotti, S. Matthies, H.R. Wenk, MAUD: a friendly Java program for material analysis using diffraction, CPD Newsl. 21 (1999) 14–15.
[54] K. Zaara, M. Chemingui, V. Optasanu, M. Khitouni, Solid solution evolution during mechanical alloying in Cu-Nb-Al compounds, Int. J. Miner. Metall. Mater. 26 (2019) 1129–1139, https://doi.org/10.1007/s12613-019-1820-y.
[55] A.D. Fortes, E. Suard, M.-H. Lemée-Cailleau, C.J. Pickard, R.J. Needs, Crystal structure of ammonia monohydrate phase II, J. Am. Chem. Soc. 131 (2009) 13508–13515.
[56] C.D. Ling, M. Avdeev, V.V. Kharton, A.A. Yaremchenko, R.B. Macquart, M. Hoelzel, Structures, phase transitions, hydration, and ionic conductivity of Ba4Ta2O9, Chem. Mater. 22 (2010) 532–540.
[57] N.W. Ashcroft, A.R. Denton, Vegard's law, Phys. Rev. A 43 (1991) 3161–3164.
[58] S. Sabbaghianrad, M. Kawasaki, T.G. Langdon, Microstructural evolution and the mechanical properties of an aluminum alloy processed by high-pressure torsion, J. Mater. Sci. 47 (2012) 7789–7795, https://doi.org/10.1007/s10853-012-6524-x.
[59] J. Wongsa-Ngam, M. Kawasaki, T.G. Langdon, Achieving homogeneity in a Cu–Zr alloy processed by high-pressure torsion, J. Mater. Sci. 47 (2012) 7782–7788, https://doi.org/10.1007/s10853-012-6587-8.
[60] K. Edalati, T. Fujioka, Z. Horita, Microstructure and mechanical properties of pure Cu processed by high-pressure torsion, Mater. Sci. Eng. A 497 (2008) 168–173, https://doi.org/10.1016/j.msea.2008.06.039.
[61] R.K. Koju, K.A. Darling, K.N. Solanki, Y. Mishin, Atomistic modeling of capillary-driven grain boundary motion in Cu-Ta alloys, Acta Mater. 148 (2018) 311–319, https://doi.org/10.1016/j.actamat.2018.01.027.
[62] M.Y. Alawadhi, S. Sabbaghianrad, Y. Huang, T.G. Langdon, Direct influence of recovery behaviour on mechanical properties in oxygen-free copper processed using different SPD techniques: HPT and ECAP, J. Mater. Res. Technol. 6 (2017) 369–377, https://doi.org/10.1016/j.jmrt.2017.05.005.